PHYSICAL REVIEW LETTERS **130,** 116204 (2023)

Connecting Higher-Order Topology with the Orbital Hall Effect in Monolayers of Transition Metal Dichalcogenides

Marcio Costa,[1,*] Bruno Focassio,[2,3] Luis M. Canonico,[4] Tarik P. Cysne,[1] Gabriel R. Schleder,[5] R. B. Muniz,[1]
Adalberto Fazzio,[2,3] and Tatiana G. Rappoport[6,7]
[1]*Instituto de Física, Universidade Federal Fluminense, 24210-346 Niterói, Rio de Janeiro, Brazil*
[2]*Federal University of ABC (UFABC), 09210-580 Santo André, São Paulo, Brazil*
[3]*Ilum School of Science, CNPEM, 13083-970 Campinas, São Paulo, Brazil*
[4]*Catalan Institute of Nanoscience and Nanotechnology (ICN2), CSIC and BIST, Campus UAB, Bellaterra, 08193 Barcelona, Spain*
[5]*John A. Paulson School of Engineering and Applied Sciences, Harvard University, Cambridge, Massachusetts 02138, USA*
[6]*Instituto de Telecomunicações, Instituto Superior Tecnico, University of Lisbon, Avenida Rovisco Pais 1, Lisboa, 1049001 Portugal*
[7]*Instituto de Física, Universidade Federal do Rio de Janeiro, Caixa Postal 68528, 21941-972 Rio de Janeiro, Rio de Janeiro, Brazil*

(Received 10 May 2022; revised 18 November 2022; accepted 13 February 2023; published 17 March 2023)

Monolayers of transition metal dichalcogenides (TMDs) in the $2H$ structural phase have been recently classified as higher-order topological insulators (HOTIs), protected by C_3 rotation symmetry. In addition, theoretical calculations show an orbital Hall plateau in the insulating gap of TMDs, characterized by an orbital Chern number. We explore the correlation between these two phenomena in TMD monolayers in two structural phases: the noncentrosymmetric $2H$ and the centrosymmetric $1T$. Using density functional theory, we confirm the characteristics of $2H$ TMDs and reveal that $1T$ TMDs are identified by a $\mathbb{Z}_4$ topological invariant. As a result, when cut along appropriate directions, they host conducting edge states, which cross their bulk energy-band gaps and can transport orbital angular momentum. Our linear response calculations thus indicate that the HOTI phase is accompanied by an orbital Hall effect. Using general symmetry arguments, we establish a connection between the two phenomena with potential implications for orbitronics and spin orbitronics.

DOI: 10.1103/PhysRevLett.130.116204

Introduction.—The orbital Hall effect (OHE) refers to the transverse flow of orbital angular momentum (OAM) in response to a longitudinally applied electric field. It resembles the spin Hall effect (SHE) [1–4], but unlike the latter, it does not require spin-orbit coupling (SOC). Characteristics of the OHE and the physical mechanisms underlying it are currently under investigation [5–10]. For instance, signatures of the OHE in 3D metallic systems were recently observed [11,12], paving the way for possible orbitronic applications [1,13,14].

Lately, the OHE in two-dimensional (2D) materials has received a great deal of attention [15–25]. Theoretical calculations predict the existence of orbital textures in some 2D materials, which can give rise to the OHE [17,18,26,27]. They have been observed in insulating transition metal dichalcogenides (TMDs) [28,29], where OHE plateaus are predicted [17–20]. Furthermore, it is possible to attribute an orbital Chern number to this insulating phase [19,20], indicating a connection with nontrivial topology.

The topological nature of layered TMDs is mostly focused on the distorted structural phase $1T'$ that hosts topological insulators [30–32]. Less is known about the topology of octahedral ($1T$) and trigonal prismatic ($2H$) structures, where most monolayers exhibit an insulating character [33]. MoS_2 is an archetype of a $2H$ TMD that exhibits a large energy band gap. Their zigzag nanoribbons display metallic edge states that cross the bulk gap [34,35], suggesting an underlying topology, despite being trivial with respect to the $\mathbb{Z}_2$ index [36].

References [37,38] have revealed that some $2H$ TMDs are 2D higher-order topological insulators (HOTIs), not previously identified by the SHE signature [39]. Triangular nanoflakes with armchair edges present in-gap corner states with fractional charge, protected by C_3 symmetry. Besides being one of the striking features of a 2D-HOTI [39–44], they explain the presence of metallic edge states in the zigzag edges and connect them to the topology of the 2D material. Their topological bulk polarization is perpendicular to the zigzag edges, leading to charge accumulation and metallic edge states.

Here, we use density functional theory (DFT) and linear-response calculations to study the interplay between the OHE and HOTI phases in monolayers of TMDs respecting the rotation symmetry C_3. We uncover that centrosymmetric $1T$ TMDs can also be HOTIs. We then correlate the appearance of a HOTI phase in the two different structures with an orbital Hall insulating phase. We discuss the existence of a pseudo-time-reversal symmetry, which originates from the crystalline symmetries of the lattice.

0031-9007/23/130(11)/116204(7)

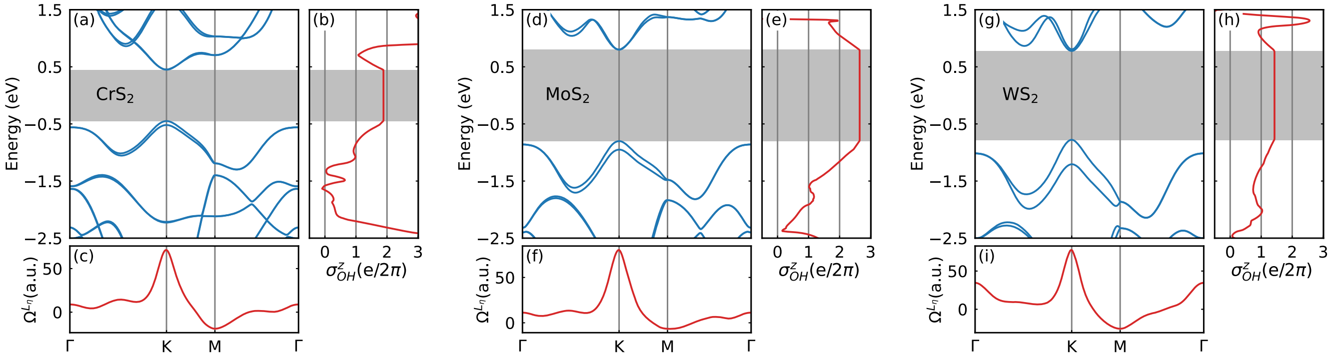

FIG. 1. $2H$-TMD monolayers of CrS$_2$, MoS$_2$, and WS$_2$ fully relativistic band structures [(a), (d), and (g)] and orbital Berry curvatures [(c), (f), and (i)], calculated along high-symmetry directions of the 2D Brillouin zone. Panels (b), (e), and (h) display the corresponding OH conductivities calculated as a function of energy.

In analogy with the photonic quantum spin Hall effect, eigenstates of the orbital angular momentum play the role of pseudospins. They are also eigenstates of the C_3 rotation operator that protects the HOTI. Because of the orbital nature of the pseudospins, the higher-order topological phase can be witnessed by the OHE. We use a well-known low energy model for HOTIs [45] and the three d-orbitals model for $2H$ TMDs [46] to explicitly show this connection [47].

OHE calculations for TMDs in the 2H and 1T structural phases.—We begin by presenting the band structure and the OHE for the two families. For that purpose, we performed DFT calculations for $1T$- and $2H$-TMD monolayers (MX_2, where M is a transition metal and X is a chalcogen). The TMD structures were obtained from the C2DB database [61]. We also adopted their criteria for dynamic (phonons) and thermodynamic stability. We fully optimize the structural parameters to obtain the wave functions. Then, we construct a PAO Hamiltonian using the pseudo-atomic-orbital (PAO) projection method [62–65] for each compound. This method is implemented in the PAOFLOW code [66,67]; for technical details see Supplemental Material (SM).

Once the PAO Hamiltonian $\mathcal{H}_{\mathrm{PAO}}(\mathbf{k})$ is built, we calculate the spin Hall (SH) and orbital Hall (OH) conductivities to linear order on the external electric field [17–19]

$$\sigma^{\eta}_{\mathrm{OH(SH)}} = \frac{e}{(2\pi)^2}\sum_n \int_{\mathrm{BZ}} d^2k f_{n\mathbf{k}}\, \Omega^{X_\eta}_{n,\mathbf{k}}, \qquad (1)$$

where $\sigma^{\eta}_{\mathrm{OH(SH)}}$ is the OH (SH) dc conductivity with polarization along the η direction, $f_{n\mathbf{k}}$ is the Fermi-Dirac distribution, and $\Omega^{X_\eta}_{n,\mathbf{k}}$ is the angular momentum projected Berry curvature in the intra-atomic approximation [17–19] (see SM [47]).

Figures 1 and 2 show the fully relativistic band structures, OH conductivities, and the orbital Berry curvatures calculated for different TMD monolayers. In Fig. 1 we depict results for $2H$ TMDs CrS$_2$, MoS$_2$, and WS$_2$. We note that within their insulating gaps these systems exhibit OH conductivity (OHC) plateaus with values $\sigma^z_{\mathrm{OH}} = 1.89$, 2.65, and 1.43 in units of $(e/2\pi)$, respectively. Conversely, σ^x_{OH} and σ^y_{OH} vanish for all three systems. Their corresponding orbital Berry curvatures are similar. They are peaked around the K point with similar maxima for the three systems, giving a large positive contribution to the OHC. Around M, the Berry curvature becomes negative

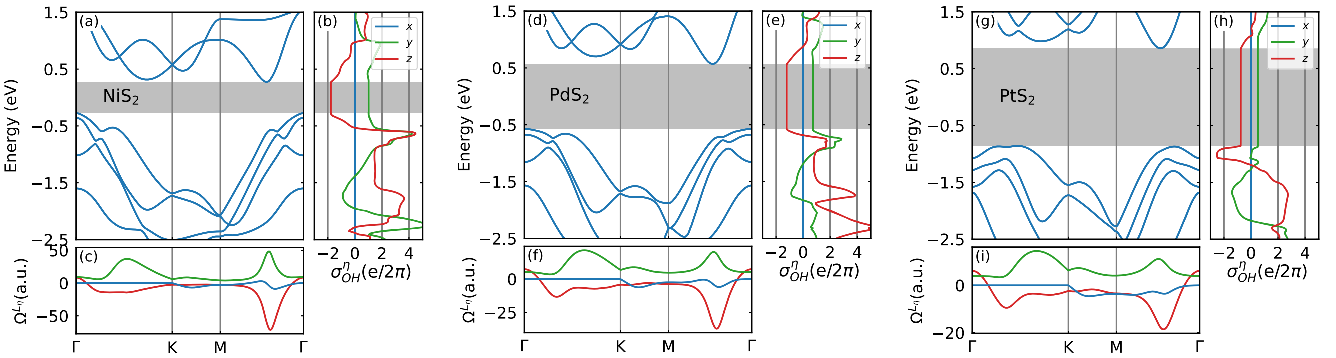

FIG. 2. $1T$ TMD monolayers of NiS$_2$, PdS$_2$, and PtS$_2$ fully relativistic band structures [(a), (d), and (g)] and orbital Berry curvatures [(c), (f), and (i)], calculated along high-symmetry directions of the 2D Brillouin zone. Panels (b), (e), and (h) display the corresponding OH conductivities calculated as a function of energy.

TABLE I. Main characteristics of the $1T$-TMD monolayers insulating phases of NiS_2, PdS_2, and PtS_2. Z_M is the atomic number of the constituent transition metal atom. The columns σ^x_{OH}, σ^y_{OH}, σ^z_{OH}, and $|\sigma_{OH}|$ show their OHE in-gap values in units of $e/(2\pi)$. E_g is the energy band gap and the last column shows the values of the topological invariant $\mathbb{Z}_4$.

TMD (Z_M)	σ^x_{OH}	σ^y_{OH}	σ^z_{OH}	$\lvert\sigma_{OH}\rvert$	E_g (eV)	$\mathbb{Z}_4$
NiS_2 (28)	0	1.02	−1.78	2.05	0.54	2
PdS_2 (46)	0	0.73	−1.22	1.85	1.14	2
PtS_2 (78) [69]	0	0.51	−0.77	0.92	1.72	2

and has different values for the three compounds, resulting in the plateau variations obtained for the OHCs when we go from Cr to W. Since the top valence bands of the TMDs have predominantly d character, the chalcogen element does not significantly affect the OHC. Table 1 of the SM [47] shows that the in-gap OHC does not change much when S is replaced by Se or Te.

Figure 2 presents results for the $1T$-TMDs monolayers NiS_2, PdS_2, and PtS_2. Differently from the $2H$ TMDs, the OHCs for the $1T$ TMDs with y polarization are not zero, and thus contribute to the entire OHC. We follow Ref. [68] and define the absolute value of the OHC as $|\sigma_{OH}| = \sqrt{(\sigma^x_{OH})^2 + (\sigma^y_{OH})^2 + (\sigma^z_{OH})^2}$. Within each energy band gap, we clearly see that the dominant contribution to $|\sigma_{OH}|$ is σ^z_{OH} for all three systems, and the OHC plateau reduces as we move from Ni to Pt.

Table I summarizes the main findings depicted in Fig. 2. It is noteworthy that both $2H$- and $1T$-TMD monolayers exhibit finite OH conductivity plateaus within their insulating energy gaps. This shows that the OHE in 2D materials is not constrained by spatial inversion symmetry and can also appear in centrosymmetric monolayers. Our results are inline with recent predictions showing that centrosymmetric $2H$-TMD bilayers also display OHC plateaus [18–20]. We note that $|\sigma_{SH}| = 0$ inside the band gap for both sets, which is consistent with the fact that TMDs do not exhibit a quantum spin Hall effect (QSHE) in the structural phases studied here. In the SM, we include tables containing several $2H$ and $1T$ semiconducting TMD monolayers [47]. We present their electronic band structures and orbital-weighted Berry curvatures for the valence bands and discuss some of their features.

HOTI phase.—We now proceed to the characterization of the HOTI phases. Recent works showed that triangular nanoflakes of $2H$-TMD monolayers with armchair edges present in-gap corner states with fractional charge $(-\frac{1}{3}|e|)$, protected by C_3 symmetry [37,38]. We begin our analysis by calculating the topological indicators for this TMD family.

For noncentrosymmetric materials, the HOTI phase is protected by a C_n rotation symmetry. It can be identified by the symmetry representations of the occupied energy bands at special high-symmetry points (HSPs) of the first Brillouin zone (BZ) [44]. For C_3 rotation symmetry, we take $[K^{(3)}_p] = \#K^{(3)}_p - \#\Gamma^{(3)}_p$, where $\#K^{(3)}_p$ and $\#\Gamma^{(3)}_p$ represent the number of occupied bands with symmetry eigenvalue $e^{2\pi i(p-1)/3}$ (for $p = 1, 2, 3$) at the K- and Γ-high-symmetry points, respectively. The final topological indicator $\chi^{(3)}$ and corner charge $Q^{(3)}_c$ are given by

$$\chi^{(3)} = ([K^{(3)}_1], [K^{(3)}_2]), Q^{(3)}_c = \frac{e}{3}[K^{(3)}_2] \bmod e, \tag{2}$$

where e is the elemental charge. We use the software IrRep [70] to calculate the symmetry eigenvalues of the occupied DFT energy bands. With them, we calculate the topological indicator and the corner charge with the expressions above. The three $2H$-TMD monolayers presented here have the same topological indicator $\chi^{(3)} = [-1, 2]$ and corner charge $Q^{(3)}_c = 2e/3$. A table for several $2H$ TMDs is included in the SM [47].

To complement the analysis based on the eigenstates of the rotation operator, we use DFT to examine $2H$-TMD triangular flakes with armchair edges and confirm the presence of in-gap corner states, as shown in Fig. 3. $2H$ TMDs also display an electronic dipole $\mathbf{P} = (\frac{1}{3}, \frac{2}{3})$, which is perpendicular to the zigzag direction [37]. As a result, if the system is cut in the zigzag direction, there is charge accumulation at the edges, leading to metallic edge states.

Differently from the $2H$ TMDs, $1T$ TMDs are HOTIs protected by inversion symmetry. Hence, they are characterized by the $\mathbb{Z}_4$ indicator, which can be calculated from the inversion parities of occupied bands [71,72]: $\mathbb{Z}_4 = \sum_{k_i \in \mathrm{TRIMs}} n_-(k_i) \bmod 4$, where $n_-(k_i)$ is the number of odd parity occupied Kramer pairs at the time-reversal invariant momenta (TRIM) points k_i in the BZ.

The index $\mathbb{Z}_4 = 2$ warrants that $1T$ TMDs also present conducting edge states capable of carrying OAM currents. This can be confirmed from the energy bands of a PtS_2 nanoribbon with zigzag edges portrayed in Fig. 4. This figure also highlights the orbital projection of the edge states. Because of the inversion symmetry, Bloch states of $1T$ TMDs do not exhibit net OAM but can still display an

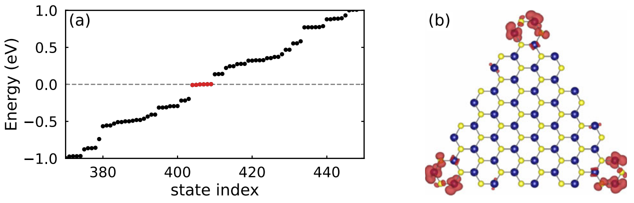

FIG. 3. Monolayer MoS_2 nanoflake (0D) geometry. (a) Fully relativistic calculation eigenvalues. The corner states are highlighted in red. (b) Real space projection of the eigenfunctions for the corner states highlighted in panel (a). Isosurface value of 0.003 e Å^{-3}.

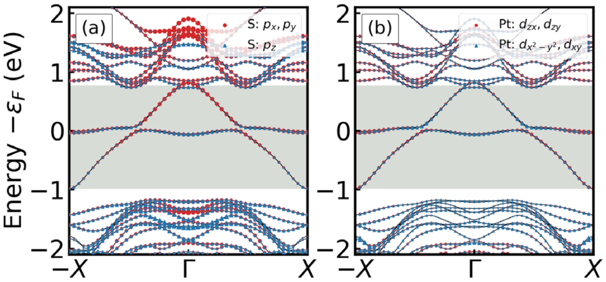

FIG. 4. Orbital projected band structures of a 18.6 Å-wide zigzag nanoribbon of a PtS_2 monolayer calculated with the PAOFLOW Hamiltonian. The shaded area and colored markers represent the bulk band gap and orbital projections, respectively. (a) Contributions from the p_x, p_y (red circles) and p_z (blue triangles) orbitals from S atoms. (b) Contributions from the d_{xz}, d_{yz} (red circles) and $d_{x^2-y^2}$, d_{xy} (blue triangles) orbitals of Pt atoms.

OHE [3]. As a result, the nanoribbon bands do not have any OAM polarization. This contrasts with the $2H$-TMD nanoribbons that have well-defined orbital-polarized edge states.

Discussion.—We have shown that a large set of insulating 2D materials exhibits a sizable OHE coexisting with a HOTI phase. This shows that higher-order topology may allow in-gap conducting edge states that can transport orbital angular momentum in the orbital Hall insulating phase. The bulk polarization perpendicular to the edges of a 2D HOTI yields to charge accumulation at the edges. As a result, these systems can have conductive edge states within their bulk energy band gaps when cut along certain directions.

To connect the OHE with the HOTI phase, it is worth recalling how the QSHE is emulated in photonic crystals. For the appearance of a $\mathbb{Z}_2$ topological phase, one needs Kramers degenerate pairs. However, bosonic systems do not possess half-integer spins. Thus, under the action of time-reversal symmetry operation ($\mathcal{T}$), they transform as $\mathcal{T}^2 = 1$, whereas for fermionic systems, $\mathcal{T}^2 = -1$ [73]. To engineer the photonic QSHE, one may construct a Hamiltonian that is invariant under inversion and a pseudo-time-reversal symmetry ($\mathcal{T}_p$) so that $\mathcal{T}_p{}^2 = -1$. This is achieved with a lattice of dielectric cylinders, which work as artificial atoms exhibiting electronic orbital-like shapes that produce the photonic bands [74]. The pseudo-time-reversal operator originates from a combination of lattice symmetry operations in such a way that the pseudospins are eigenstates of L_z such as $p_\pm = p_x \pm i p_y$ and $d_\pm = d_{xy} \pm i d_{x^2-y^2}$ [74,75].

To identify these pseudospins in the TMDs, we can use general symmetry considerations regarding 2D materials with threefold rotational symmetry. The crystal field in low-dimensional systems leads to large splittings between orbitals, inducing the formation of energy gaps. However, the rotational symmetry also imposes constraints on the energy states. These have to be also eigenstates of the rotation operator at the high symmetry points.

For $2H$ TMDs, the conduction and valence bands at K and K' are mainly composed of d_{z^2} and $d_\pm$ orbitals, which are eigenstates of L_z. This is a consequence of the D_{3h} point group symmetry of the crystal: the d_{z^2} orbitals belong to the unidimensional irreducible representation A_1, while the d_{xy} and $d_{x^2-y^2}$ belong to E'. Since the representation E' is two dimensional, the linear combinations $d_\pm$ can be treated as pseudospins that transform under a pseudo-time-reversal symmetry operator related to the rotation operators. In the SM [47], we show that the Chern number associated with $\mathcal{T}_p$ symmetry leads to the same result previously obtained [19].

In the case of the $1T$ TMDs, the identification of the pseudospins is more subtle. The D_{3d} symmetry imposes that the p orbitals of the X atoms and the d orbitals from the M atom should be dominant for the bulk energy states near Γ. Our first-principles calculations [47] evince a strong energy splitting in Γ between the p_x, p_y and the p_z orbitals, as previously reported by Yao *et al.* for PtSe_2 [76]. The valence and conduction bands near the gap have a strong contribution of linear combinations of p_x and p_y orbitals of the X atom that form $p_\pm$, which transform as $\mathcal{T}_p{}^2 = -1$. They are also composed of $d_\pm$. The sizable contribution of d_{xz} and d_{yz} orbitals explains the L_y component of the OHE. When the system is cut into a ribbon, these orbitals participate in the formation of edge states, as shown in Fig. 4(b). Therefore, in contrast with $2H$ TMDs, these edge states will be mainly composed of combinations of three pseudospins, one formed by the p_x, p_y orbitals and two composed of the d_{xz}, d_{yz}, $d_{x^2-y^2}$, and d_{xy} orbitals.

In principle, similar to photonics systems, one could use these eigenstates of L_z to emulate topological phases in fermionic materials: a system which is invariant under inversion and $\mathcal{T}_p$, must have pseudospins forming Kramers' pairs. However, differently from bosons, fermions have half-integer spins, and two spin-degenerate states for each pseudospin. Therefore, if one tries to construct a fermionic system without spin-orbit coupling where the pseudospins emulate a quantum spin Hall insulator, the system has spin-degenerate pseudospins Kramers' pairs. This results in an even number of Kramers' pairs and the system cannot be indexed by a $\mathbb{Z}_2 = 1$, although it can be a HOTI.

To illustrate these ideas, we use the low energy Hamiltonian presented in Ref. [45] to model HOTIs protected by C_3 rotation and inversion symmetries (see SM [47]). This model consists of a block diagonal Hamiltonian containing basically the superposition of two copies of the Bernevig-Hughes-Zhang (BHZ) model. It is well known that each BHZ Hamiltonian presents a $\mathbb{Z}_2$ topological phase. Its eigenstates can also be written in terms of pseudospins that are eigenstates of L_z. Surprisingly, we show they present an orbital Hall plateau in their topological gap. When the two BHZ copies are taken into account, the system is not a topological insulator but, as shown in Ref. [45], it is a HOTI that has twice the number of edge states of the BHZ model. As expected, the HOTI still presents an orbital Hall plateau and the orbital current can be carried by the in-gap edge states.

To strengthen this link, we used another model to show the onset of a HOTI phase in systems without inversion symmetry, following the ideas presented in Ref. [77]. We considered the simplified three orbital tight-binding Hamiltonian in a triangular lattice that describes the low-energy properties of $2H$ TMDs. We begin with a case with inversion symmetry and orthogonality between the orbitals in different representations. Under this condition, a strong spin-orbit coupling opens a gap in the system, leading to a trivial insulator phase with a vanishing OHE and the absence of in-gap edge states. From this, we identify that if inversion symmetry is broken and hopping between orthogonal orbitals is allowed, as in the case of $2H$ TMD, there is a topological transition to a HOTI that presents zigzag metallic edge states and a large OH plateau, which is independent of the SOC [47].

Conclusions.—We employed DFT and linear response transport calculations to study the interplay between the orbital Hall effect and higher-order topological phases. We analyzed all stable $2H$ or $1T$ monolayer TMDs and found that they are HOTIs, protected by either C_3 rotation symmetry ($2H$) or inversion symmetry ($1T$). Simultaneously, they all display a plateau in the orbital Hall conductivity inside the band gap.

Recent works start to uncover the role of orbital hybridization in HOTIs and the advent of orbital effects [77–79]. Here, we connect the HOTI phase to the existence of pseudo-time-reversal operators and associated pseudospinors. As these pseudospinors are eigenstates of the orbital angular momentum, HOTI phases can generate an OHE. More importantly, HOTIs with edges that are perpendicular to their bulk polarization present in-gap metallic edge states that can carry the orbital angular momentum in the orbital Hall insulating phase. This can be employed for efficient orbital current injection in novel spin-orbitronics devices. Furthermore, the OHE in 2D HOTIs may be used in machine learning strategies for spotting potentially useful materials for orbitronic applications [80–82].

We acknowledge CNPq/Brazil, CAPES/Brazil, FAPERJ/Brazil, INCT Nanocarbono and INCT Materials Informatics for financial support. T. G. R. acknowledges funding from Fundação para a Ciência e a Tecnologia and Instituto de Telecomunicações—Grant No. UID/50008/2020 in the framework of the project Sym-Break. M. C. acknowledges CNPq (Grant No. 317320/2021-1) FAPERJ/Brazil (Grant No. E26/200.240/2023) and the National Laboratory for Scientific Computing (LNCC/MCTI, Brazil) for providing HPC resources. B. F. acknowledges funding from FAPESP/Brazil under Grant No. 2019/04527-0 and the Brazilian Nanotechnology National Laboratory (LNNano/CNPEM, Brazil) for computational resources. A. F. acknowledges funding from FAPESP/Brazil under Grant No. 2017/02317-2. L. M. C. acknowledges the funding from the ECONWHET project, reference PID2019-106684GBI00, funded by MCIN/AEI/10.13039/501100011033/ and by “ERDF A way of making Europe.” ICN2 is funded by the CERCA Programme/Generalitat de Catalunya and supported by the Severo Ochoa Centres of Excellence program, funded by the Spanish Research Agency (Grant No. SEV-2017-0706).

---

[*] mjtcosta@id.uff.br

[1] D. Go, D. Jo, H.-W. Lee, M. Kläui, and Y. Mokrousov, Europhys. Lett. **135**, 37001 (2021).

[2] B. A. Bernevig, T. L. Hughes, and S.-C. Zhang, Phys. Rev. Lett. **95**, 066601 (2005).

[3] D. Go, D. Jo, C. Kim, and H.-W. Lee, Phys. Rev. Lett. **121**, 086602 (2018).

[4] D. Jo, D. Go, and H.-W. Lee, Phys. Rev. B **98**, 214405 (2018).

[5] L. Salemi and P. M. Oppeneer, Phys. Rev. Mater. **6**, 095001 (2022).

[6] L. Salemi and P. M. Oppeneer, Phys. Rev. B **106**, 024410 (2022).

[7] L. Salemi, M. Berritta, and P. M. Oppeneer, Phys. Rev. Mater. **5**, 074407 (2021).

[8] P. Sahu, S. Bhowal, and S. Satpathy, Phys. Rev. B **103**, 085113 (2021).

[9] I. Baek and H.-W. Lee, Phys. Rev. B **104**, 245204 (2021).

[10] H. Lee, B. Choi, and H.-W. Lee, Phys. Rev. B **105**, 035142 (2022).

[11] Y.-G. Choi, D. Jo, K.-H. Ko, D. Go, K.-H. Kim, H. G. Park, C. Kim, B.-C. Min, G.-M. Choi, and H.-W. Lee, arXiv:2109.14847.

[12] D. Lee, D. Go, H.-J. Park, W. Jeong, H.-W. Ko, D. Yun, D. Jo, S. Lee, G. Go, J. H. Oh *et al.*, Nat. Commun. **12**, 6710 (2021).

[13] S. Park and B.-J. Yang, Nano Lett. **20**, 7694 (2020).

[14] D. Go, D. Jo, T. Gao, K. Ando, S. Blügel, H.-W. Lee, and Y. Mokrousov, Phys. Rev. B **103**, L121113 (2021).

[15] F. Xue, V. Amin, and P. M. Haney, Phys. Rev. B **102**, 161103(R) (2020).

[16] T. P. Cysne, F. S. M. Guimarães, L. M. Canonico, T. G. Rappoport, and R. B. Muniz, Phys. Rev. B **104**, 165403 (2021).

[17] L. M. Canonico, T. P. Cysne, T. G. Rappoport, and R. B. Muniz, Phys. Rev. B **101**, 075429 (2020).

[18] L. M. Canonico, T. P. Cysne, A. Molina-Sanchez, R. B. Muniz, and T. G. Rappoport, Phys. Rev. B **101**, 161409(R) (2020).

[19] T. P. Cysne, M. Costa, L. M. Canonico, M. B. Nardelli, R. B. Muniz, and T. G. Rappoport, Phys. Rev. Lett. **126**, 056601 (2021).

[20] T. P. Cysne, S. Bhowal, G. Vignale, and T. G. Rappoport, Phys. Rev. B **105**, 195421 (2022).

[21] V. o. T. Phong, Z. Addison, S. Ahn, H. Min, R. Agarwal, and E. J. Mele, Phys. Rev. Lett. **123**, 236403 (2019).

[22] S. Bhowal and S. Satpathy, Phys. Rev. B **102**, 035409 (2020).

[23] S. Bhowal and G. Vignale, Phys. Rev. B **103**, 195309 (2021).

[24] X. Mu, Y. Pan, and J. Zhou, npj Comput. Mater. **7**, 61 (2021).

[25] Y. Shi and J. Zhou, Phys. Rev. B **104**, 155146 (2021).

[26] F. C. de Lima, G. J. Ferreira, and R. H. Miwa, Nano Lett. **19**, 6564 (2019).

[27] L. M. Canonico, T. G. Rappoport, and R. B. Muniz, Phys. Rev. Lett. **122**, 196601 (2019).

[28] S. Beaulieu, J. Schusser, S. Dong, M. Schüler, T. Pincelli, M. Dendzik, J. Maklar, A. Neef, H. Ebert, K. Hricovini *et al.*, Phys. Rev. Lett. **125**, 216404 (2020).

[29] S. Beaulieu, M. Schüler, J. Schusser, S. Dong, T. Pincelli, J. Maklar, A. Neef, F. Reinert, M. Wolf, L. Rettig *et al.*, npj Quantum Mater. **6**, 93 (2021).

[30] X. Qian, J. Liu, L. Fu, and J. Li, Science **346**, 1344 (2014).

[31] S. Tang, C. Zhang, D. Wong, Z. Pedramrazi, H.-Z. Tsai, C. Jia, B. Moritz, M. Claassen, H. Ryu, S. Kahn *et al.*, Nat. Phys. **13**, 683 (2017).

[32] F. Giustino, J. H. Lee, F. Trier, M. Bibes, S. M. Winter, R. Valentí, Y.-W. Son, L. Taillefer, C. Heil, A. I. Figueroa *et al.*, J. Phys. **3**, 042006 (2020).

[33] S. Manzeli, D. Ovchinnikov, D. Pasquier, O. V. Yazyev, and A. Kis, Nat. Rev. Mater. **2**, 17033 (2017).

[34] E. Ridolfi, L. R. F. Lima, E. R. Mucciolo, and C. H. Lewenkopf, Phys. Rev. B **95**, 035430 (2017).

[35] H. Rostami, R. Asgari, and F. Guinea, J. Phys. Condens. Matter **28**, 495001 (2016).

[36] T. Frank, P. Högl, M. Gmitra, D. Kochan, and J. Fabian, Phys. Rev. Lett. **120**, 156402 (2018).

[37] J. Zeng, H. Liu, H. Jiang, Q.-F. Sun, and X. C. Xie, Phys. Rev. B **104**, L161108 (2021).

[38] S. Qian, G.-B. Liu, C.-C. Liu, and Y. Yao, Phys. Rev. B **105**, 045417 (2022).

[39] M. Costa, G. R. Schleder, C. M. Acosta, A. C. M. Padilha, F. Cerasoli, M. B. Nardelli, and A. Fazzio, npj Comput. Mater. **7**, 49 (2021).

[40] R.-J. Slager, L. Rademaker, J. Zaanen, and L. Balents, Phys. Rev. B **92**, 085126 (2015).

[41] W. A. Benalcazar, B. A. Bernevig, and T. L. Hughes, Science **357**, 61 (2017).

[42] W. A. Benalcazar, B. A. Bernevig, and T. L. Hughes, Phys. Rev. B **96**, 245115 (2017).

[43] Z. Song, Z. Fang, and C. Fang, Phys. Rev. Lett. **119**, 246402 (2017).

[44] W. A. Benalcazar, T. Li, and T. L. Hughes, Phys. Rev. B **99**, 245151 (2019).

[45] F. Schindler, Z. Wang, M. G. Vergniory, A. M. Cook, A. Murani, S. Sengupta, A. Y. Kasumov, R. Deblock, S. Jeon, I. Drozdov *et al.*, Nat. Phys. **14**, 918 (2018).

[46] G.-B. Liu, W.-Y. Shan, Y. Yao, W. Yao, and D. Xiao, Phys. Rev. B **88**, 085433 (2013).

[47] See Supplemental Material at http://link.aps.org/supplemental/10.1103/PhysRevLett.130.116204 which includes Refs. [48–60], for (A) methodology (B) band structure, orbital Hall conductivity and orbital Berry curvature for a larger set of $2H$ and $1T$ monolayer TMDs (C) Low energy model and (D) three bands model for HOTIs with finite orbital Hall conductivity. (E) Effect of an hBN substrate on the orbital Hall conductivity.

[48] P. Hohenberg and W. Kohn, Phys. Rev. **136**, B864 (1964).

[49] W. Kohn and L. J. Sham, Phys. Rev. **140**, A1133 (1965).

[50] P. Giannozzi, O. Andreussi, T. Brumme, O. Bunau, M. Buongiorno Nardelli, M. Calandra, R. Car, C. Cavazzoni, D. Ceresoli, M. Cococcioni *et al.*, J. Phys. Condens. Matter **29**, 465901 (2017).

[51] J. P. Perdew, K. Burke, and M. Ernzerhof, Phys. Rev. Lett. **77**, 3865 (1996).

[52] G. Kresse and D. Joubert, Phys. Rev. B **59**, 1758 (1999).

[53] A. Dal Corso, Comput. Mater. Sci. **95**, 337 (2014).

[54] M. Costa, G. R. Schleder, M. Buongiorno Nardelli, C. Lewenkopf, and A. Fazzio, Nano Lett. **19**, 8941 (2019).

[55] M. Costa, A. T. Costa, W. A. Freitas, T. M. Schmidt, M. Buongiorno Nardelli, and A. Fazzio, ACS Omega **3**, 15900 (2018).

[56] M. Costa, M. B. Nardelli, A. Fazzio, and A. T. Costa, arXiv:1808.00347.

[57] M. Costa, N. M. R. Peres, J. Fernández-Rossier, and A. T. Costa, Phys. Rev. B **102**, 014450 (2020).

[58] J. J. Heath, M. Costa, M. Buongiorno-Nardelli, and M. A. Kuroda, Phys. Rev. B **101**, 195439 (2020).

[59] L. Fu and C. L. Kane, Phys. Rev. B **76**, 045302 (2007).

[60] J. Mei, Z. Chen, and Y. Wu, Sci. Rep. **6**, 1 (2016).

[61] S. Haastrup, M. Strange, M. Pandey, T. Deilmann, P. S. Schmidt, N. F. Hinsche, M. N. Gjerding, D. Torelli, P. M. Larsen, A. C. Riis-Jensen *et al.*, 2D Mater. **5**, 042002 (2018).

[62] L. A. Agapito, A. Ferretti, A. Calzolari, S. Curtarolo, and M. Buongiorno Nardelli, Phys. Rev. B **88**, 165127 (2013).

[63] L. A. Agapito, S. Curtarolo, and M. Buongiorno Nardelli, Phys. Rev. X **5**, 011006 (2015).

[64] L. A. Agapito, M. Fornari, D. Ceresoli, A. Ferretti, S. Curtarolo, and M. B. Nardelli, Phys. Rev. B **93**, 125137 (2016).

[65] L. A. Agapito, S. Ismail-Beigi, S. Curtarolo, M. Fornari, and M. B. Nardelli, Phys. Rev. B **93**, 035104 (2016).

[66] M. Buongiorno Nardelli, F. T. Cerasoli, M. Costa, S. Curtarolo, R. D. Gennaro, M. Fornari, L. Liyanage, A. R. Supka, and H. Wang, Comput. Mater. Sci. **143**, 462 (2018).

[67] F. T. Cerasoli, A. R. Supka, A. Jayaraj, M. Costa, I. Siloi, J. Sławińska, S. Curtarolo, M. Fornari, D. Ceresoli, and M. Buongiorno Nardelli, Comput. Mater. Sci. **200**, 110828 (2021).

[68] J. H. Garcia, M. Vila, C.-H. Hsu, X. Waintal, V. M. Pereira, and S. Roche, Phys. Rev. Lett. **125**, 256603 (2020).

[69] Y. Zhao, J. Qiao, P. Yu, Z. Hu, Z. Lin, S. P. Lau, Z. Liu, W. Ji, and Y. Chai, Adv. Mater. **28**, 2399 (2016).

[70] M. Iraola, J. L. Mañes, B. Bradlyn, M. K. Horton, T. Neupert, M. G. Vergniory, and S. S. Tsirkin, Comput. Phys. Commun. **272**, 108226 (2022).

[71] J. Kruthoff, J. de Boer, J. van Wezel, C. L. Kane, and R.-J. Slager, Phys. Rev. X **7**, 041069 (2017).

[72] E. Khalaf, H. C. Po, A. Vishwanath, and H. Watanabe, Phys. Rev. X **8**, 031070 (2018).

[73] T. Ozawa, H. M. Price, A. Amo, N. Goldman, M. Hafezi, L. Lu, M. C. Rechtsman, D. Schuster, J. Simon, O. Zilberberg *et al.*, Rev. Mod. Phys. **91**, 015006 (2019).

[74] L.-H. Wu and X. Hu, Phys. Rev. Lett. **114**, 223901 (2015).

[75] J. Mei, Z. Chen, and Y. Wu, Sci. Rep. **6**, 32752 (2016).

[76] W. Yao, E. Wang, H. Huang, K. Deng, M. Yan, K. Zhang, K. Miyamoto, T. Okuda, L. Li, Y. Wang *et al.*, Nat. Commun. **8**, 14216 (2017).

[77] P. Eck, Y. Fang, D. Di Sante, G. Sangiovanni, and J. Cano, arXiv:2207.01359.

[78] M. Mazanov and M. A. Gorlach, Phys. Rev. B **105**, 205117 (2022).

[79] J. Gliozzi, M. Lin, and T. L. Hughes, arXiv:2211.08438.

[80] G. R. Schleder, B. Focassio, and A. Fazzio, Appl. Phys. Rev. **8**, 031409 (2021).

[81] G. R. Schleder, C. M. Acosta, and A. Fazzio, ACS Appl. Mater. Interfaces **12**, 20149 (2019).

[82] G. R. Schleder, A. C. M. Padilha, A. R. Rocha, G. M. Dalpian, and A. Fazzio, J. Chem. Inf. Model. **60**, 452 (2019).